In-Orbit Assessment of a Physics-based Star Tracker Model Using DART and PSP Flight Data

Scott E. Miller (1), Mark Pittelkau (2), Emil Superfin (1), Dan O'Shaughnessy (1)

(1) DART GNC Engineer, Johns Hopkins University Applied Physics Laboratory, 11100 Johns Hopkins Road, Laurel MD 20723

(2) GNC Consultant, Aerospace Control Systems LLC, 35215 Greyfriar Drive, Round Hill, VA 20141

ABSTRACT

A physics-based star tracker noise model was developed to mitigate risk on NASA's recent Double Asteroid Redirection Test (DART) mission, whose targeting errors were highly sensitive to tracker noise. The modeling approach captures lens distortion residuals and other low spatial frequency errors via a set of two-dimensional polynomials. A triangular-wave centroiding error model was used to emulate high spatial frequency errors (HSFE). White noise was introduced to emulate random measurement errors and QUEST is used for batch quaternion estimation. A hybrid model is also developed in which the HSFE centroiding error model was replaced with a first-order Gauss-Markov process. The LSFE parameters are derived from vendor-supplied optical distortion data. HSFE and temporal noise parameters are estimated from flight data obtained from NASA's Parker Solar Probe (PSP) mission, which flies two Leonardo AA-STR star trackers that are identical to the DART tracker. The hybrid model was shown to underperform in scenarios in which the angular rates were subject to discrete changes, and its model parameters required recalibration for each operational case. The physical modeling approach led to a medium fidelity model that functioned well in all test cases without requiring recalibration and is therefore preferred.

1 INTRODUCTION

Star trackers are highly accurate attitude sensors that often play a central role in meeting spacecraft mission requirements. Star trackers efficiently convert two-dimensional star centroid data into a 3D attitude vector by comparing centroids against a resident star catalog, and using a sequential or batch estimation method such as QUEST [1]. Errors are generated by a multitude of sources that include optical distortion effects, color aberration, shutter effects, misalignments, and image motion. High fidelity error modeling is not only complex, but is often made more difficult due to the proprietary technical aspects of a given design [2].

The DART spacecraft was built by the Johns Hopkins Applied Physics Laboratory (APL) and launched in 2021 to demonstrate asteroid hazard mitigation via kinetic deflection at realistic planetary scales. DART successfully served as a kinetic deflector as it impacted the asteroid Dimorphos, the secondary member of the Didymos binary asteroid system, thereby altering the orbit of Dimorphos with respect to Didymos. The single Leonardo AA-STR on board the DART spacecraft was critical to the success of the mission, which required precise attitude knowledge to autonomously intercept Dimorphos at an approach speed of 6.1 km/sec. Developing an accurate tracker noise model for use in a terminal phase emulation was therefore a paramount concern. A thorough description of the DART mission from a GNC perspective is found in Ref. [3].

This paper focuses on two tracker modeling approaches that were employed to emulate flight performance on NASA's recent NASA's Double Asteroid Redirection Test (DART) mission. The first method captures the most salient aspects of the underlying physical processes responsible for generating noise using a parsimonious set of parameters that includes standard deviations for low spatial frequency errors (LSFE), high spatial frequency errors (HSFE), and temporal noise (TN). These parameters are commonly provided by the star tracker manufacturer, but can also be determined through calibration testing. The second approach is a hybrid method that empirically fits spectral data to a first-order Gauss Markov (FOGM) process through an optimization process, while still employing a lens distortion model. This hybrid approach is sensitive to the operational environment since the first-order Markov assumption is generally not representative of the noise process, and requires ground or flight data to compute its parameters. However, the DART mission was able to benefit from flight test data obtained from two identical trackers on APL's Parker Space Probe (PSP) mission to calibrate the model.

This paper presents both modeling methodologies and then assesses their performance against flight data obtained from the PSP and DART spacecraft in a variety of operational configurations. The physics-based approach is described in Section 2 and the FOGM-based hybrid method is presented in Section 3. In-flight performance is then evaluated against an Inertial Hold Test performed on PSP (Section 4.1), a PSP IMU Calibration activity (Section 4.2), and a DART Pre-Impact Terminal Test (Section 4.3).

2 PHYSICS-BASED NOISE MODEL (PBM)

2.1 Background

Star tracker noise may be broadly categorized as Temporal Noise, High Spatial Frequency Error, Low Spatial Frequency Error, and bias (static and quasi-static) [4]. Biases are actively estimated and removed by the spacecraft's attitude determination algorithm. The TN is white Gaussian error that spans a frequency range from zero to the Nyquist frequency (half of the sampling frequency). HSFE is primarily due to centroiding error caused by spatial sampling of the star image and is periodic with the pixel spacing [5]. HSFE is also caused by pixel response non-uniformity and noise non-uniformity, and by distortion of the point spread function. The HSFE is caused mainly by centroiding error and varies spatially as a star traverses the pixels on the focal plane. LSFE arises due to lens distortion, chromatic refraction, thermal scaling, focal length changes, the degradation of charge transfer efficiency (in CCD detectors), rolling shutter compensation errors (in rolling shutter APS detectors), and other effects [5]. LSFE varies spatially over the focal plane.

The temporal manifestation of both HSFE and LSFE depends on the motion of the stars on the focal plane. If the stars are not moving, the HSFE and LSFE appear as biases. If the stars move at a constant rate, the HSFE manifests as cyclical errors at a fundamental frequency and its harmonics while the LSFE varies according to the star motion on the focal plane. If the stars move cyclically over only a few pixels, the centroiding error is cyclic while the LSFE is effectively static. If the star motion is cyclic across a large region of the focal array then the distortion-induced error is also cyclic and contains a bias (the distortion residual at the mean operating point) that depends on the star pattern. The cyclical error amplitude is reduced as a function of the number of stars tracked, and is less than the mean distortion residual.

2.2 Modeling Approach

A parsimonious physical modeling approach is taken in which key error contributors are captured using a minimum set of parameters. A fully-detailed high-fidelity physical model would include several additional error sources, such as motion-induced error due to finite exposure times, radiometric errors, and shutter effects. The approach described here instead relies on only a small set of parameters that includes the pixel dimensions of the focal plane, the FOV, and the standard deviations for LSFE, HSFE, and TN commonly provided by the star tracker manufacturer. These standard deviations are per-star circular values that are best derived from test data, rather than specification values. Generic specification values advertised by the manufacturer are upper bounds on performance under specified operating conditions.

The physics-based model (PBM) described herein applies LSFE, HSFE, and TN to the ideal centroid positions of each star in the star field at a given frame. A quaternion measurement is then realized using the QUEST batch attitude estimation algorithm [1]. The temporal noise is modeled trivially as a normal Gaussian distribution with a standard deviation σ_{TN}. The LSFE and HSFE effects are rigorously characterized in the next subsections, followed by a brief description of the batch attitude estimation processing.

2.3 Distortion Errors (LSFE)

The focal plane geometry of the star tracker is shown in Figure 1 ([6]). The *i*-th star vector w_i in the imaging frame (X,Y,Z) is defined as

$$w_i = \begin{bmatrix} x_i \\ y_i \\ f \end{bmatrix} \qquad (1)$$

where *f* is the camera's focal length and (x_i, y_i) is the ideal location of the *i*-th centroid on the focal plane. Aberrations in the optical system distort the geometric image of the *i*-th star on the focal plane such that its true location $(x_i{}', y_i{}')$ is given as

$$\begin{aligned} x_i' &= x_i + \Delta x_i \\ y_i' &= y_i + \Delta y_i \end{aligned} \qquad (2)$$

where $(\Delta x_i, \Delta y_i)$ is the distortion error associated with the *i*-th star. Manufacturers typically use optical testing to generate 2D calibration polynomials $(\Delta\bar{x}, \Delta\bar{y})$ that approximate distortion anywhere on the focal plane as a function of position. These polynomials are typically 2nd or 3rd order. The distortion correction from optical measurements of the CT-602 tracker that flew on the MSX mission [7] is represented as a quiver plot in Figure 2. Applying the *i*-th centroid distortion correction $(\Delta\bar{x}_i, \Delta\bar{y}_i)$ to Eq. (2), the above expression may be restated as

$$\begin{aligned} x_i' &= x_i + \Delta\bar{x}_i + \epsilon_x^i \\ y_i' &= y_i + \Delta\bar{y}_i + \epsilon_y^i \end{aligned} \qquad (3)$$

where $(\epsilon_x^i, \epsilon_y^i)$ is the residual distortion correction error.

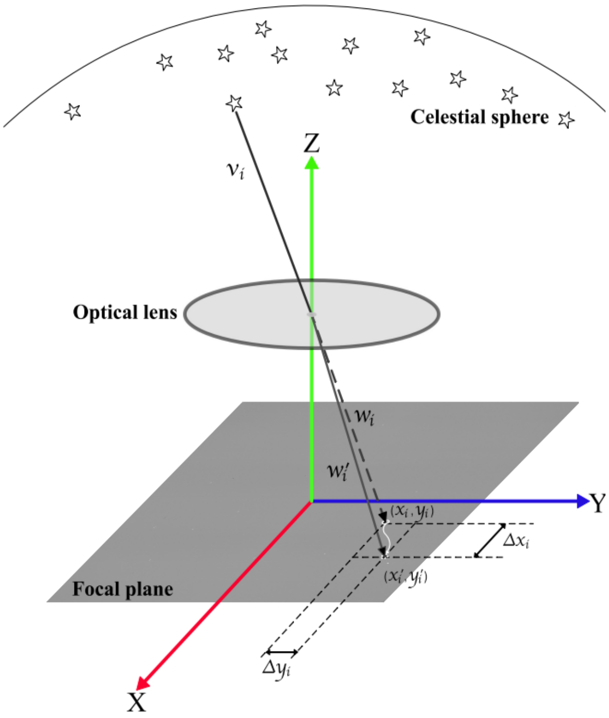

Figure 1. Star Tracker geometry (graphic from Ref. [6]).

Following the approach of Ref. [8], the distortion residual error (ϵ_x, ϵ_y) at any location (x, y) in the focal plane may be approximated by a pair of distortion functions $F_1(x, y)$ and $F_2(x, y)$, i.e.

$$\begin{aligned} \epsilon_x &= \epsilon_x(x, y) \approx F_1(x, y) \\ \epsilon_y &= \epsilon_y(x, y) \approx F_2(x, y) \end{aligned} \tag{4}$$

where

$$F_1(x, y) = \sum_{j=0}^{\mathrm{M}} \sum_{k=0}^{\mathrm{N}} a_{ij} x^j y^k \ , \qquad F_2(x, y) = \sum_{j=0}^{\mathrm{M}} \sum_{k=0}^{\mathrm{N}} b_{jk} x^j y^k \tag{5}$$

Eq. (5) may be represented in matrix-vector form by first defining the vectors

$$\begin{aligned} \boldsymbol{x} &= [1 \ \ x \ \ x^2 \ \ \cdots \ \ x^M]^T \\ \boldsymbol{y} &= [1 \ \ y \ \ y^2 \ \ \cdots \ \ y^N]^T \end{aligned} \tag{6}$$

and matrices

$$\boldsymbol{A} = \begin{bmatrix} a_{0,0} & \cdots & a_{0,M} \\ \vdots & \ddots & \vdots \\ a_{N,0} & \cdots & a_{N,M} \end{bmatrix}, \qquad \boldsymbol{B} = \begin{bmatrix} b_{0,0} & \cdots & b_{0,M} \\ \vdots & \ddots & \vdots \\ b_{N,0} & \cdots & b_{N,M} \end{bmatrix} \tag{7}$$

The residual distortion polynomials at the *i*-th centroid location (x_i, y_i) are then found by computing

$$\begin{aligned} F_1(x_i, y_i) &= \boldsymbol{y}_{\boldsymbol{i}}^T \boldsymbol{A} \boldsymbol{x}_{\boldsymbol{i}} \\ F_2(x_i, y_i) &= \boldsymbol{y}_{\boldsymbol{i}}^T \boldsymbol{B} \boldsymbol{x}_{\boldsymbol{i}} \end{aligned} \tag{8}$$

where $(\boldsymbol{x}_{\boldsymbol{i}}, \boldsymbol{y}_{\boldsymbol{i}})$ are evaluated directly from Eq. (6) at the *i*-th centroid coordinate. It is convenient to set M = N. We have chosen $M = N = 7$.

Because the distortion residuals are not known, the coefficient matrices ($\boldsymbol{A}$ and $\boldsymbol{B}$) are randomly drawn from a (zero-mean, unit variance) normal distribution. The random selection of coefficients yields an arbitrary RMS error, so the coefficient matrices must be scaled such that the total RMS distortion error is consistent with the manufacturer-specified LSFE deviation σ_{LSF}. The scaling is accomplished by performing a rectangular integration over a fine mesh to compute the means and distortion coefficient matrix variances (σ_A, σ_B). The mean is subtracted from the zero-order elements $(a_{0,0}, b_{0,0})$ and then the shifted $\boldsymbol{A}$ and $\boldsymbol{B}$ matrices are respectively scaled by $(\sigma_{LSF}/\sigma_A)/\sqrt{2}$ and $(\sigma_{LSF}/\sigma_B)/\sqrt{2}$ (the $\sqrt{2}$ factor is necessary to dilute the circular σ_{LSF} specification into per-axis values). Although the numerical integration requires significant computation, it is only performed once during the model initialization.

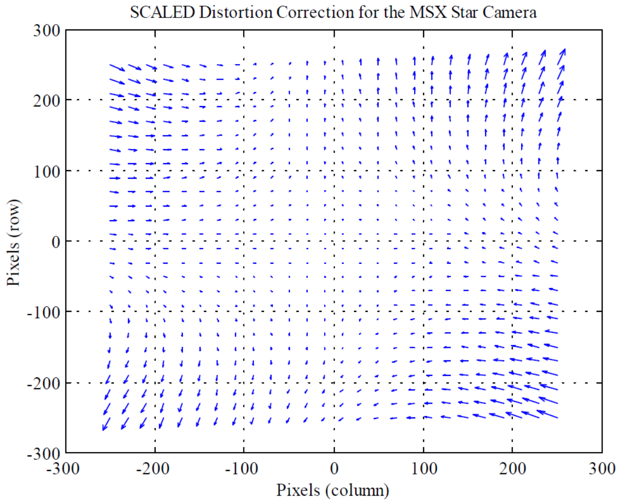

Figure 2. Distortion Corrections for the MSX CT-602 star tracker, obtained through optical testing.

2.4 Centroiding Errors (HSFE)

Ideally the point spread function (PSF) of the optics is symmetric and covers a 3 × 3 grid of pixels. Centroiding error is due to the discrete sampling and windowing of the star image, and PSF distortion. If smear due to image motion is negligible, these errors are spatially periodic with a spatial period equal to the pixel spacing. This is illustrated in Figure 3, which was obtained from acceptance test data in which a simulated star image is moved across the FOV of the Ball CT-601 tracker [9]. The observed centroid error is a triangular function that is spatially periodic at the pixel spacing length.

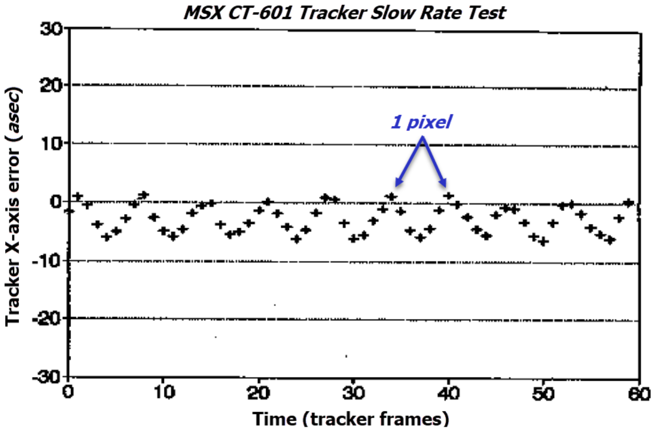

Figure 3. Centroiding error, as measured for a CT-601 tracker flown on MSX.

To model the centroiding error, it is convenient to rescale the focal plane coordinates (x, y) such that the star positions are represented in pixel coordinates, i.e.

$$(P_x, P_y) = \left(\frac{kM_p}{2}x\,, \frac{kN_p}{2}y\right) \tag{9}$$

for an $M_p \times N_p$ array of pixels, where the scale factor k serves to normalize the focal plane coordinates such that $(kx, ky) \in [-1,1]$. Based on Figure 3, the per-axis centroiding errors $\left(c_x, c_y\right)$ are modeled as triangle waves, i.e.

$$c_x(\phi_x) = \sigma_{HSF}\frac{2}{\pi}\operatorname{asin}(\sin(\phi_x)), \qquad c_y\left(\phi_y\right) = \sigma_{HSF}\frac{2}{\pi}\operatorname{asin}(\sin(\phi_y)) \tag{10}$$

where σ_{HSF} is the circular RMS error and

$$\begin{aligned} \phi_x &= 2\pi \operatorname{rem}(P_x, 1) \\ \phi_y &= 2\pi \operatorname{rem}\left(P_y, 1\right) \end{aligned} \tag{11}$$

are the phase angles of the centroid between adjacent pixels.

2.5 Attitude Solution

The measured attitude quaternion output from the star tracker is determined using the QUEST algorithm [1], although other algorithms could be used as well [10]. The measurement vector w_i of the i-th star in a star field containing M stars was given in Eq. (1). The QUEST algorithm returns the quaternion associated with the attitude matrix $\boldsymbol{C}$ that minimizes the weighted mean-square error

$$\boldsymbol{L}(\boldsymbol{C}) = \sum_{i=1}^{M} \frac{1}{\sigma_i^2}\left|\hat{w}_i - \boldsymbol{C}\hat{v}_i^2\right|^2 \tag{12}$$

where $\hat{w}_i = w_i/|w_i|$, $\hat{v}_i$ is the true unit vector to the i-th star (obtained from a star catalog), and σ_i^2 is error variance of the i-th star measurement. σ_i^2 is the zero-mean sum of both measurement and catalog position error variances. The measured star vector is related to the catalog star vector through the estimated attitude matrix plus an estimation error e_i:

$$\hat{v}_i = \boldsymbol{C}\hat{w}_i + e_i \tag{13}$$

The covariance of the attitude estimation error in $\boldsymbol{C}$ is

$$\boldsymbol{P} = \sigma^2 \left[\boldsymbol{I} - \sum_{i=1}^{M} \frac{1}{\sigma_i^2} \widehat{w}_i \widehat{w}_i^T \right]^{-1}, \qquad \frac{1}{\sigma^2} = \sum_{i=1}^{M} \frac{1}{\sigma_i^2} \tag{14}$$

For lack of information to compute the measurement error variance, it is often assumed that the centroiding errors are statistically isotropic so that the variances are equal for every star.

2.6 Model Implementation

Figure 4 describes how the PBM is implemented. In the k'th processing step a truth quaternion $(q_I^{ST})^{true}$ is provided as an input to the algorithm, which prescribes the orientation of the star tracker's local frame of reference with respect to the J2000 inertial frame. To return the measurement quaternion $(q_I^{ST})^{meas}$ the algorithm performs the following steps:

> *Step 1: Update the Star Field.* Star trackers contain proprietary algorithms that manage which catalogued stars are tracked. Our model can use either externally-supplied star locations or an internal algorithm to generate a star field. The algorithm checks the positions of the tracked stars at each time step to confirm that the star images are within the focal plane. A star that exits the FOV is replaced with a new star whose image is in the focal plane and not already tracked. Our replacement algorithm avoids clustering by randomly selecting new stars inside a bounding box centered at $(-x_c, -y_c)$, where (x_c, y_c) represents the mean location of all remaining tracked stars. The bounding box is sized to be fully contained within the FOV and no larger than the standard deviation of the distribution of the remaining stars.
>
> *Step 2: Apply Distortion Model.* The set of true (distortion-corrected) star positions on the focal plane w_k^{true} are moved via Eq. (8) to adjusted locations w_k^{LSFE} that include LSFE distortion residual errors. The residual distortion matrices (Eq. (7)) are pre-defined at initialization through a random draw using the approach described above in Section 2.3.
>
> *Step 3: Apply Centroiding Errors.* Centroiding errors are applied to the star locations w_k^{LSFE} using Eq. (10). These errors are sized per the parameter σ_{HSF}.
>
> *Step 4: Apply Temporal Noise.* Temporal noise is added to each star based on normal Gaussian distribution with a standard deviation σ_{TN}. Note that σ_{TN} is implicitly defined as a *per-star* circular deviation here, rather than a measure of angular error as is typically provided. To convert an angular-derived σ_{TN} value to a per-star value, the angular value should be scaled by a factor $f/\sqrt{M}$, where f is the focal length and M is the number of star centroids used in the attitude solution.
>
> *Step 5: Apply QUEST.* Use QUEST [1] to compute the star tracker quaternion, $(q_I^{ST})^{meas}$.

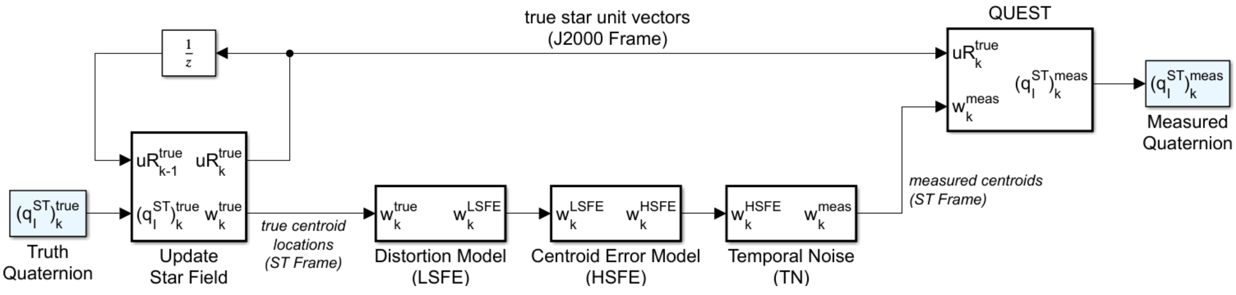

Figure 4. Physics-based Model (PBM) implementation.

3 HYBRID EMPIRICAL NOISE MODEL (HEM)

Under certain operational conditions it is possible to characterize star tracker noise using a hybrid approach that uses the LSFE distortion model described in Section 2.3, but replaces the HSFE centroiding model described in Section 2.4 with a first-order Gauss-Markov (FOGM) process. Employing this type of hybrid model substantially reduces computational throughput as it avoids the need to apply the centroiding error corrections (Eq. (10)) to each individual star at every frame processing step (note that the LSFE distortion model is implemented as a single matrix multiply operation). The drawback of exercising a hybrid model is nonetheless significant: it may only be used reliably under a restricted set of operational scenarios in which the underlying FOGM assumptions are valid. This usually implies that the star field moves at a constant rate across the field of view.

3.1 HEM Model Derivation

For the HEM, HSFE and TN effects are emulated as a stationary first-order Gauss-Markov process model with an autocorrelation function given by

$$R(\tau) = \sigma_{HSF}^2 \, e^{-\tau/\tau_{HSF}} + \sigma_{TN}^2 \, \delta_o(\tau) \tag{15}$$

where $\delta_o(\tau)$ is a Dirac measure for which

$$\delta_o(\tau) = \begin{cases} 1 & \tau = 0, \\ 0 & \text{otherwise} \end{cases} . \tag{16}$$

The FOGM process is governed by a variance σ_{HSF}^2 and exponential autocorrelation time constant τ_{HSF}. Temporal noise is represented as an uncorrelated zero-mean Gaussian sequence with a variance σ_{TN}^2. Defining f_s as the sample frequency, the one-sided Power Spectral Density (PSD) for the process governed by Eq. (15) is then [11]

$$\boldsymbol{\Phi}(\boldsymbol{f}) = \left(\frac{2\,\tau_{HSF}}{(2\pi\boldsymbol{f}\;\tau_{HSF})^2+1}\right)\sigma_{HSF}^2 + \left(\frac{2}{f_s}\right)\sigma_{TN}^2 \tag{17}$$

where $\boldsymbol{f} = [f_1 \; \cdots f_N]^T$ is an N-dimensional column vector of discrete frequencies whose *k*'th element $\boldsymbol{f}_k \in [0, \pi f_s)$.

Eq. (15) is the underpinning assumption that restricts the model's usage as noted above. The FOGM model assumes that the HSFE is a stationary process governed by an exponential autocorrelation function. Centroiding errors manifest as a result of the discrete sampling of each star's PSF, which inherently is not a stationary process. However, if the star field traverses the focal plane of the array with a constant rate and direction then the HSFE angular error may be reasonably characterized by a FOGM equivalent model. Under certain operating conditions a FOGM equivalent process model can be found that will reasonably match the tracker's true noise characteristics. This is discussed further in Section 4.

3.2 Implementation

The complete hybrid model combines Eq. (15) with the LSFE distortion effects, as is shown in Figure 5. The constant K_o scales the output such that the PSD of the HSFE FOGM block matches the PSD of the HSFE term in the preceding equation. The discrete processing period is defined as *T*. The model parameters σ_{HSF}, τ_{HSF}, and σ_{TN} can be estimated from the PSD of data containing the star tracker residual errors. Let the error defined at each discrete frequency contained in $\boldsymbol{f}$ be described by the vector

$$\boldsymbol{e} = [e_1 \; \cdots e_N]^T \, . \tag{18}$$

Defining the PSD of the star tracker flight data residual estimates as $\boldsymbol{\Phi_o}(\boldsymbol{f})$, the optimal model parameters are found by minimizing the cost function

$$\mathcal{J}(\boldsymbol{f}, \sigma_{TN}, \sigma_{HSF}, \tau_{HSF}) = \mathbf{e}^{\mathrm{T}}\mathbf{e} \tag{19}$$

where

$$\boldsymbol{e}_k \triangleq \log \boldsymbol{\Phi}(\boldsymbol{f}_k) - \log \boldsymbol{\Phi}_{\mathbf{o}}(\boldsymbol{f}_k) \tag{20}$$

Since the PSDs at low frequencies are less accurate due to the number of samples in the data set, Eq. (20) uses the log operator to provide a coherent fit across the entire spectrum by de-weighting the cost in proportion to frequency.

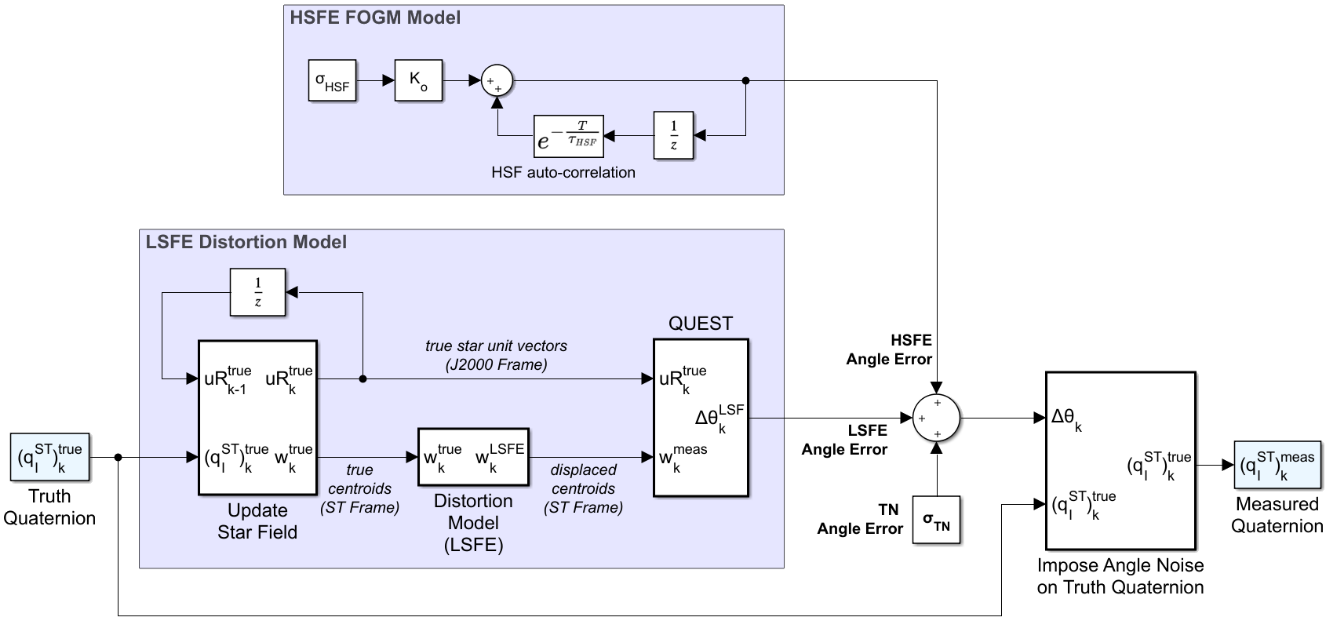

Figure 5. Hybrid Empirical Model that combines an empirical FOGM noise model with a physical optical distortion model.

4 IN-FLIGHT MODEL PERFORMANCE

The primary motivation for this study was to develop a star tracker noise model that would be predictive of the Leonardo AASTR star tracker performance flown on the DART mission during the mission's terminal encounter with Dimorphos. The two AASTR trackers currently employed on the Parker Solar Probe (PSP) mission are effectively identical to the DART unit. The operational availability of PSP for tracker testing provided the DART team with a unique opportunity to fine-tune the tracker model in a flight environment. The primary objectives of PSP tracker tests were to

1. *Experimentally determine model parameters.* Only the LSFE deviation σ_{LSF} was explicitly determined by Leonardo through optical testing of the PSP units, but the HSFE deviation σ_{HSF} was not. A PSP "Inertial Hold Test" (IHT) was therefore designed to empirically derive values for the use in both the physics-based centroiding algorithm (Section 2.4) and the FOGM algorithm (Section 3). The IHT test maintained a quasi-inertially fixed attitude over several hours, which rendered the LSFE as a bias. IHT also served to provide some advance indication of DART's AASTR performance during terminal operations, although significant operational differences between PSP and DART detracted from this comparison.

2. *Experimentally validate the physics-based noise model.* PSP regularly performs a calibration activity to remove static biases from its attitude solution. The IMU calibration procedure (Section 4.2) involves a series of slew maneuvers with intervening inertial holds. Star tracker data collected during these tests are ideal for validating the tracker noise model, since the command sequences cause the star field to traverse the FOV at various rates and directions.
3. *Compare and contrast the physics-based and hybrid empirical models.* PSP testing provided an opportunity to assess the performance of both modeling approaches. Results show that the physics-based approach is broadly applicable, while the FOGM approach leads to a lower fidelity model that is accurate in certain use cases but inaccurate in others.

4.1 PSP Inertial Hold Test

PBM and HEM parameters were derived from flight data obtained directly from the PSP spacecraft while in an operational configuration resembling DART's Terminal Phase, referred to as the PSP "Inertial Hold Test" (IHT). During the test, PSP maintained a nominal attitude while in a thermally quiescent state in order to avoid thermal transients. PSP collected high-rate sensor data while in a quasi-inertial-hold attitude that drifted with the orbit by about 9 pixels (0.166°) over approximately four hours. Because the spanned pixel distance was short and the traversal rate was slow, the LSFE was nearly static. The HSFE varied cyclically, spanning over 4.7 pixels with a period of 765 seconds per cycle in the x-direction, and 7.4 pixels with a period of 486.5 seconds in the y-direction. The test configuration therefore allowed the HSFE and TN characteristics of the tracker to be evaluated independently of the LSFE.

Table 1. AA-STR Specifications

Parameter	*Value*
FOV	20° x 20° 1024 x 1024 pixels
# Tracked Stars	Up to 15
Update Rate	10 Hz
Bias	8.25 arcsec, 3σ (cross-axis) 11.1 arcsec, 3σ (boresight)
LSFE	3.3 arcsec, 3σ (cross-axis) 15.6 arcsec, 3σ (boresight)
NEA (random error) @ 0.1 °/sec track rate	6 arcsec, 3σ (cross-axis) 49.4 arcsec, 3σ (boresight)

PSP employs two AA-STRs, referred to as ST1 and ST2. Key performance specifications for the AA-STR, as provided by Leonardo, are shown in Table 1. Measurements from both trackers are combined with angular rate measurements from a Northrop-Grumman SSIRU via an extended Kalman Filter (EKF) to provide an attitude estimate accurate to within 2 arcsec, 3σ, neglecting static misalignments. The Power Spectral Density (PSD) of the EKF estimate (after rotation into the ST1 frame) is shown in Figure 6. The mode at 0.036 Hz appears at the crossover frequency of the closed loop control system, and is due to the interaction of the controller with various noise sources. PSP's precision pointing and highly accurate attitude estimate allow for star tracker residual errors to be determined directly by differencing the tracker centroids from centroids predicted by the EKF solution.

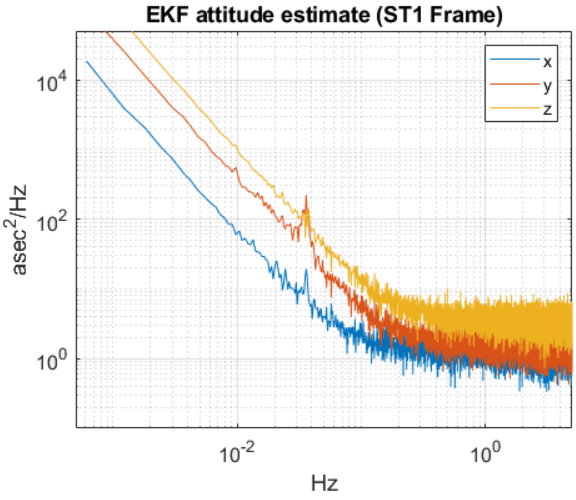

Figure 6. PSD of EKF attitude estimate, resolved in ST1 frame.

Figure 7 shows the ST1 centroid locations as reported from PSP telemetry during the 4-hour test. The AASTR's FOV is expressed in normalized focal plane coordinates such that $(x, y) \in [-1,1]$. The 14 centroid positions tracked by ST1 moved uniformly in a straight-line trajectory, traversing 8.78 pixels in 4 hours at a constant rate with very little deviation from a straight line.

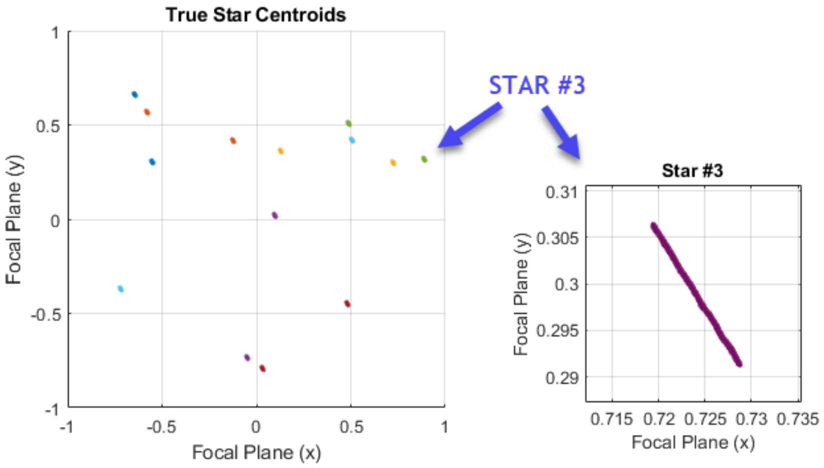

Figure 7. ST1 star centroid locations during the PSP Inertial Hold Test.

A spectral analysis was performed on the tracker residual errors and then used to evaluate the physics-based and hybrid empirical modeling approaches. The ST1 results are shown in Figure 8 (ST2 results were similar). The *blue* curves are the PSDs of the measured tracker residuals. The HEM (*magenta*) curves were obtained using the FOGM parameter estimates derived through the minimization of Eq. (19). The estimated boresight parameters are $\sigma_{HSF} = 5.06$ arcsec, $\sigma_{TN} = 7.43$ arcsec, and $\tau_{HSF} = 161$ seconds. The PBM (*red*) curve was obtained using the approach defined in Section 2 using these values for σ_{HSF} and σ_{TN}.

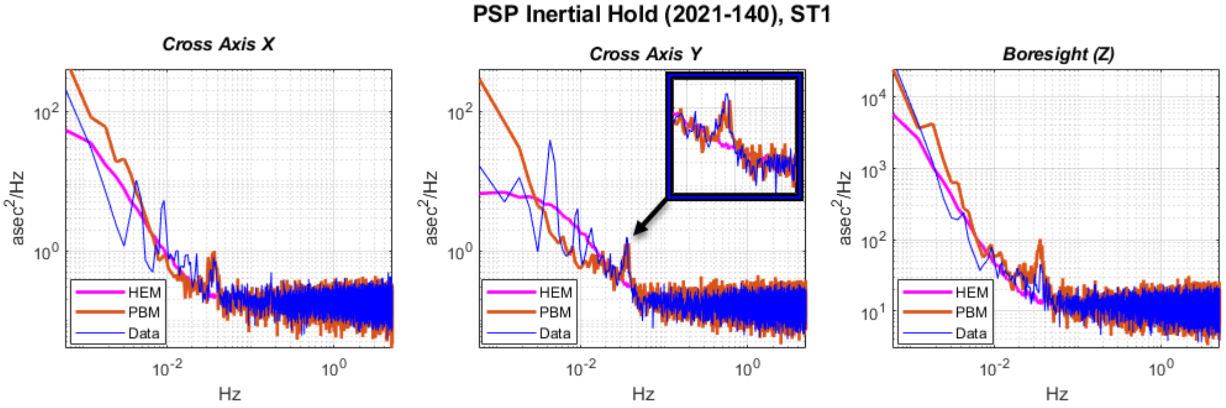

Figure 8. PSDs obtained from ST1 during the PSP Inertial Hold Test. The PBM spectrum (magenta) closely matches the measured residual error (blue) at 0.036 Hz (inset). The HEM (magenta) does not capture the effect.

The physics-based model uses the star centroid positions reported in telemetry, whose locations vary according to the true dynamic motion of the spacecraft. Therefore the 0.036 Hz dynamic mode shown above in Figure 6 is evident both in the measured residual error and in the PBM result (see Figure 8, inset). The hybrid model does not contain the signature since the centroiding error is estimated empirically, without direct dependency on the centroid locations.

4.2 PSP IMU Calibration Test (ICT)

The PSP spacecraft routinely performs a calibration activity to maintain the alignment of its star tracker frame axes with the IMU frame. The IMU calibration scheme, based on [12], requires that the spacecraft undergoes a series of orthogonal rate slews that follow the profile shown in Figure 9. During slew events the stars traverse the FOV at a maximum rate of 12 pixels/sec, which gives rise to optical distortion effects (LSFE) that are a significant contributor to total error. Between slew events a star traverses the star tracker's FOV at a rate of 0.18 pixels/sec. The directions in which each star traverses the FOV change abruptly when slews are initiated, which leads to the discontinuities seen in Figure 10.

Data was obtained from both PSP trackers during two ICT events, ICT1 on 8/17/2020 and ICT2 on 12/5/2020. The results presented here are from ST1 during ICT1; similar results were obtained during ICT2. ST1 and ST2 results closely matched each other in all cases.

Figure 9. Slews performed during PSP IMU Calibration.

The PBM and HEM share the identical optical distortion model, differing only with regard to whether the HSFE is described as a physical mechanism (PBM) or an empirical fit to existing data (HEM). The order of the distortion model was set to seven, i.e. $M = N = 7$ in Eq. (6). The LSFE per-axis circular deviation σ_{LSF} was set to 3.1667, which is the vendor-supplied value determined through optical testing. The ensuing analysis is based on results acquired from 100 randomly drawn residual distortion error matrices (Eq. (7)).

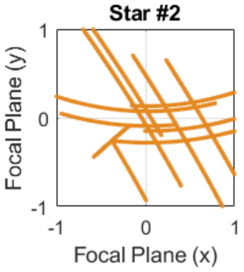

Figure 10. Star#2 measured centroid locations.

4.2.1 ICT1 Results: Physics-Based Model

The power spectral densities generated using the PBM approach are compared to the PSD of the ST1 measured filter residuals in Figure 11. The PBM used the IHT-derived σ_{HSF} and σ_{TN} values ($\sigma_{HSF} = 5.06$, $\sigma_{TN} = 7.43$ arcsec). The 100 randomly-drawn model variants are shown in grey. The mean and 3σ upper bound of those run cases are respectively plotted in red and purple. The PSD of the measured residual error is shown in light blue.

Figure 11 shows that the physics-based is consistent with the measured noise characteristics of the tracker. The LSFE is a significant contributor during the calibration test. A single random distortion model is unlikely to match the measured star tracker residual, although the model is scaled to yield the RMS error of the residual. But on average the distortion model yields a PSD that is close to the PSD of the measured error.

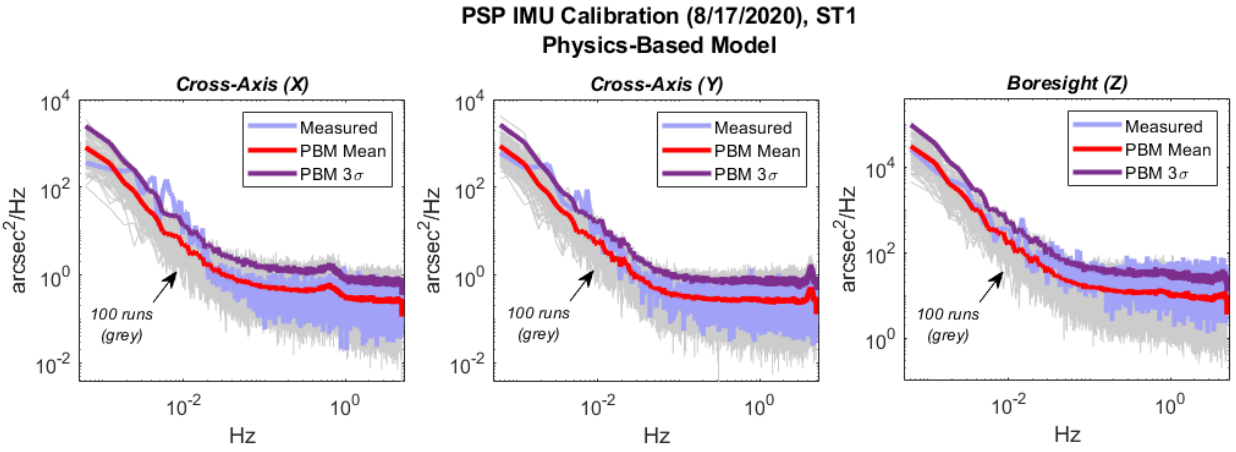

Figure 11. ICT1 PBM Results for ST1. !00 residual distortion model variants were generated (grey): the mean (red) and 3σ upper bound (purple) spectral noise are contrasted against the PSD of the ST1 measured residual error (light blue).

The PBM model does not capture the low-frequency peaks in the PSD of the star tracker data, such as the peak at 0.006 Hz in the x and y axes seen in Figure 11. This may be because the current PBM model does not include other sources of LSFE, such as image smear or rolling shutter effects inherent to the Active Pixel Sensor (APS). Turn-around error is also induced when the motion of a star field changes direction during an exposure interval. These unmodeled sources of error will be considered for future improvements of the model.

4.2.2 ICT1 Results: Hybrid Empirical Model

In Figure 12, the power spectral densities generated using the hybrid empirical modeling approach are compared to the PSD of the ST1 measured residual error during ICT1. When using the IHT-derived parameters, the HEM generates a PSD (black) that underestimates the PSD obtained through direct measurement (light blue). New FOGM parameters were therefore estimated from the ICT1 data using the curve-fitting approach as defined in Eqs. (19) and (20). The (boresight-axis) optimization yielded $\sigma_{HSF} = 5.22$ arcsec, $\sigma_{TN} = 9.37$ arcsec, and $\tau_{HSF} = 27.5$ seconds. The new σ_{HSF} and σ_{TN} are somewhat larger than the parameter estimated from IHT data, but the new τ_{HSF} is significantly less than the τ_{HSF} estimated from IHT data. Since the star tracker error is not a first-order Gauss-Markov process, the FOGM model in the HEM will typically require a different set of parameters for different pointing motion profiles. The physics-based PBM approach normally does not require a new parameter set for different operating conditions. When using the parameters estimated from the IHT, the HEM severely underestimates the PSD of the star tracker data (Figure 12). When using the new parameters from ICT1, also shown in Figure 12, the HEM more closely matches the PSD of the star tracker data but underestimates the spectrum at low frequencies. In contrast, as shown in Sections 4.1 and 4.2.1, the physics-based model yields PSDs that are close to that of the measured tracker residual errors.

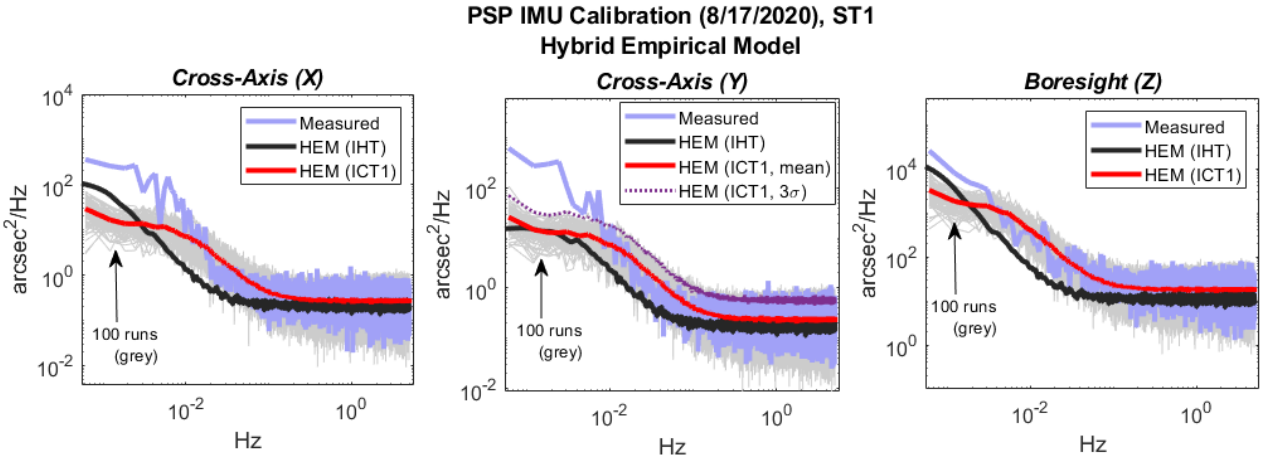

Figure 12. ICT1 HEM Results for ST1. 100 residual distortion model variants were run (grey). The mean (red) and 3σ upper bound (purple) are contrasted against the PSD of the ST1 measured residual error (light blue). The IHT HEM model is shown in green..

A Monte Carlo analysis reveals other weaknesses in the hybrid approach. Even after retuning, the HEM significantly under-predicts the noise in the low spectrum (< 0.01 Hz) while over-predicting the noise in the mid-spectrum (0.01 – 0.1 Hz). The HEM curve-fitting approach minimizes the overall fit error at the expense of matching the spectral shape. The curve fit assumes that the spectral shape is governed by a first-order exponentially-decaying autocorrelation function (Eq. (15)), which poorly represents the ICT operational environment. The physics-based model, on the other hand, is able to reasonably match both the shape and magnitude through mimicking the tracker's physical attributes.

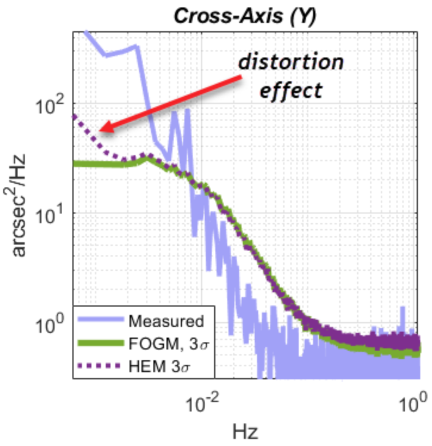

Figure 13. HEM results with the distortion model enabled (purple) and disabled (green).

Figure 13 shows how the addition of lens distortion effects (LSFE) improves the fidelity of the hybrid model. Only the y-axis ST1 data is shown, and ICT1-derived HEM parameters are used to generate the curves. The "FOGM" (green) line in the figure is the 3σ bounding curve produced for a 100-run analysis with the distortion model *disabled*. The HEM model (dotted) is the same as that shown above in Figure 12 (center), for which the distortion model was *enabled*. The distortion model improves the model's fidelity at frequencies below 0.003 Hz. The HEM otherwise produces a spectral signature that is dictated by the first order Gauss-Markov process model.

4.3 DART Pre-Impact Terminal Test (PITT)

In this section the PBM and HEM approaches are assessed against data acquired from a Pre-Impact Terminal Test (PITT)[1] performed on the DART spacecraft on July 25, 2022. The test emulated the operational environment during DART's terminal engagement with the Didymos system. The sun angle geometry and spacecraft thermal environment were maintained throughout the 2.9-hour test to closely match the terminal phase of the DART mission. Spacecraft heaters were cycled at a rate of 0.0055 Hz (3-minute period), which will become relevant in the discussion to follow.

4.3.1 DART Control System Overview

DART's control architecture differed substantially from PSP. A detailed description of DART's GNC and *Small-body Maneuvering Autonomous Real-Time Navigation* (SMART Nav) logic is provided in [3]. In general terms the GNC logic was responsible for providing time keeping, sensor and instrument data ingestion, attitude and ΔV estimation, guidance and control, gimbaled antenna and solar array pointing, and fault detection. SMART Nav logic was responsible for guiding the spacecraft onto a collision course with Dimorphos in the final four hours of flight. Functionality was distributed across firmware and software to provide image processing, asteroid targeting, trajectory guidance, and maneuver logic.

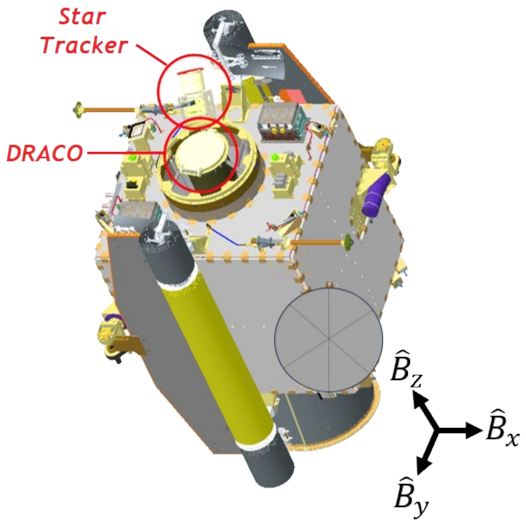

Figure 14. DART sensor and instrument locations.

DART's GNC subsystem employed a single Leonardo AA-STR (ST1). Measurements from the AA-STR were combined with angular rate measurements from a Honeywell Miniature IMU (MIMU) via an extended Kalman Filter (EKF) to provide an attitude estimate. Pointing control was maintained exclusively via a thruster-based phase plane controller: during terminal phase the attitude deadbands were set respectively to $\pm 0.11^o$ and $\pm 0.27^o$ about the cross-axes (B_x, B_y) and boresight $(-B_z)$ of the DRACO navigational camera as shown in Figure 14. The AA-STR boresight was canted 15^o away from the DRACO boresight as shown.

---

[1] also referred to as "Thermal Test 2" in Ref. [3].

The use of a single tracker, the MIMU's poor drift characteristics, and thruster-only control made it impossible to determine star tracker error residuals directly from the EKF solution as was done for PSP (see [3] for further details). The DRACO attitude solution was therefore used as an alternative. DRACO is a narrow FOV optical sensor with a 2560 x 2160 pixel focal plane and 0.29^o FOV: its flight-measured attitude uncertainty was found to be 1.5 and 124 arcsec respectively about the cross-axes and boresight (3σ). When rotated into the tracker frame, DRACO's 3σ attitude uncertainty manifests as (32, 1.5, 120) arcsec in the tracker's local (*X, Y, Z)* coordinate frame as defined in Figure 1. While the *Y*-axis measurement errors were sufficiently small, the *X* and *Z*-axis errors are too large to provide useful residual error measurements. The model assessments in this section therefore are provided for the *Y*-axis only.

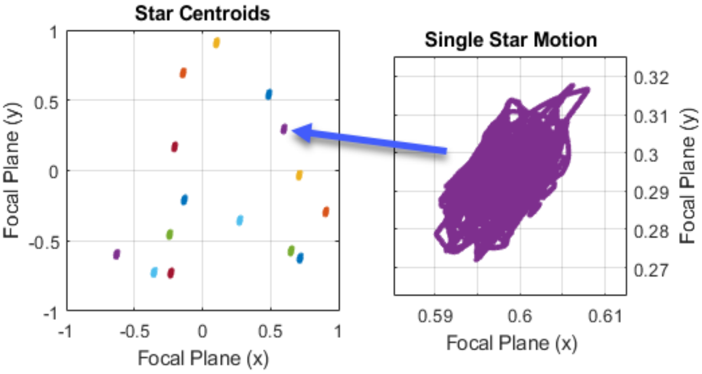

Figure 15. Star centroid locations during the DART Pre-Impact Thermal Test.

During the Pre-Impact Terminal Test (PITT) the DART spacecraft maintained an inertially-fixed attitude under thruster control as described above. The star centroid motion as measured during the test are shown in Figure 15. On average the centroid locations migrated approximately 6.5 pixels during the 2.9 hour test in a manner consistent with the PSP Inertial Hold Test (Section 4.1, see Figure 7). During IHT, however, the motion of individual stars followed straight-line tracks due to tight RWA control. Here the star motion is chaotic: phase-plane thruster control causes the star field to move rapidly in short tracks across the deadband, and the track directions change randomly. The "dithering" of the star field gives rise to spectral noise whose signature is significantly different than what was observed during the IHT event, as will now be discussed.

4.3.2 PITT Results: Physics-Based Model

The power spectral densities generated using the PBM approach are compared to the PSD of the ST1 y-axis measured residual error in Figure 16. The 100 randomly-drawn model variants are shown in grey, their mean is plotted in red, and the PSD of the measured residual error is shown in blue. The PBM used the measured centroid locations reported in the AA-STR telemetry to emulate the noise present on the tracker's estimate of the attitude quaternion. The IHT-derived σ_{HSF} and σ_{TN} values ($\sigma_{HSF} = 5.06$, $\sigma_{TN} = 7.43$ arcsec) were implemented without retuning.

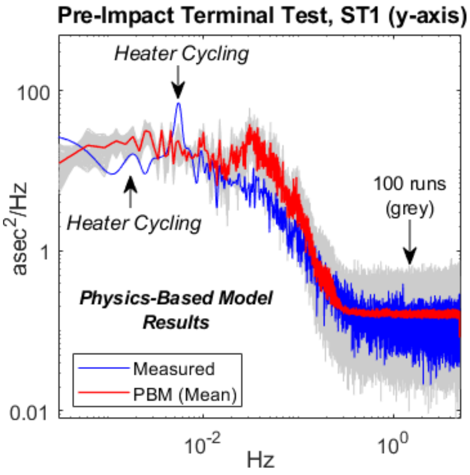

Figure 16. PBM spectrum vs. the measured residual error observed during PITT (y-axis).

The measured residual error (blue) was formed by differencing the ST1 and DRACO raw quaternion measurements, as discussed above. The low frequency spatial error is modulated by the cyclical motion associated with the thruster deadband control cycle. DRACO's thermostatically-controlled heaters, which were cycled every 3 minutes (0.0055 Hz), gave rise to thermally-induced deformation errors between the ST and DRACO frames.

Any mismatch between the measured residual error and the PBM is largely attributable to distinctions between how the measured residual and the PBM results are formed. Because the measured residual represents the relative motion between

DRACO and the AA-STR, some spectral noise that is passed through the EKF attitude estimate affects both units and so does not appear in the measured residual. The PBM directly generates spectral noise present in the tracker's attitude estimate, independent of DRACO. The PBM therefore includes spectral noise passed through by the EKF in the relative measurement, but is insensitive to thermally-induced misalignment errors.

4.3.3 PITT Results: Hybrid Empirical Model

The power spectral densities generated using the HEM approach are compared to the PSD of the ST1 y-axis measured residual error in Figure 17. The figure shows the original (PSP-derived) IHT model (green) and a re-tuned model (magenta) whose parameters were updated to fit the data set. The IHT and PITT operational conditions are nearly identical except that thruster control is used for PITT rather than RWA control. In spite of the operational similarities, the HEM model derived for IHT was clearly proven inadequate. The HEM approach attempts to find a corresponding first-order Markov process that optimally matches the data set. The random "dithering" motion of the star field under thruster deadband control during PITT generates spectral noise that cannot be approximated by the same Markov process used to model the IHT data. Hence the IHT-derived HEM cannot describe the PITT data even though both operational scenarios share significant commonality.

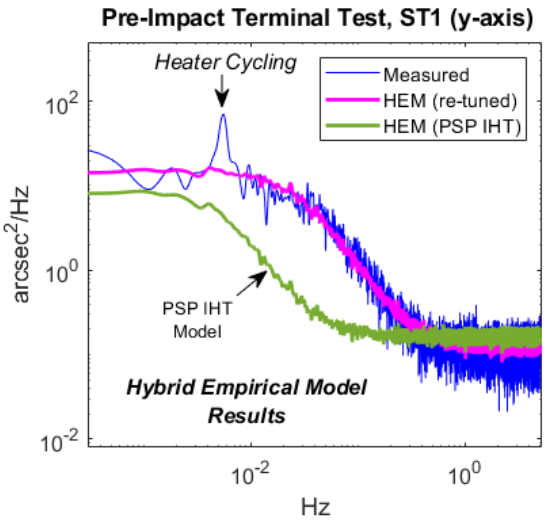

Figure 17. HEM spectrum vs. the measured residual error observed during DART PITT (y-axis).

Although the re-tuned HEM model fits the data set quite well, the ability to generate appropriate model parameters requires real tracker data obtained under a specific set of operational conditions. A HEM model developed for a particular operational environment cannot be expected to perform well in a different scenario, even if many similarities exist between them. The HEM approach therefore is not recommended for use as as generic representation of centroiding error.

5 SUMMARY

Two star tracker noise modeling approaches were described in this study, and their efficacy was examined using flight data obtained from identical AA-STR trackers flown on the PSP and DART missions. The physics-based modeling approach utilizes a physical model to describe a limited set of noise processes, e.g. optical distortion and centroiding errors. The approach requires only a small set of parameters that includes noise variances, FOV dimensions, and the number of stars tracked. The empirical approach utilizes a FOGM process model to empirically describe a given data set, and includes a physics-based distortion model for additional fidelity.

An Inertial Hold Test (IHT) performed on the PSP spacecraft was designed to directly obtain the centroiding error and temporal noise statistics needed for both models (LSFE variance had been previously determined via optical bench testing). The IHT configuration effectively eliminated optical distortion effects by maintaining an inertially fixed attitude over several hours. PSP's precise attitude control and knowledge accuracy made it possible to obtain star residual error data by comparing raw tracker measured quaternions to the EKF solution. Both models performed well, but the HEM lacked the fidelity to capture some spectral characteristics.

Both models were then compared against flight data extracted from a PSP IMU Calibration Test (ICT). The ICT event, with its multiple large-angle slews, generated both optical distortion and centroiding errors. The PBM performed adequately using the IHT-derived parameters. Some marginal limitations in the model were noted that were attributed to unmodeled effects such as turn-around error. The HEM, however, could not match the measured power spectrum without parametric retuning. The HEM approach attempts to empirically fit a given dataset to a Markov process model; since the tracker noise is not a Markov process, the HEM parameters generally are unique to each operational scenario. The HEM still underperformed even after updating its parameters.

The DART Pre-Impact Terminal Test (PITT) resembled IHT in most respects except that thrusters were used instead of RWAs. Phase-plane control gave rise to dithering within the attitude deadbands. Under these conditions the HEM was again seen to fail without parametric retuning, while the PBM approach worked well as a medium-fidelity model with some noted limitations. The PBM is recommended as a general approach for modeling tracker noise. The inclusion of unmodeled noise mechanisms, such as smear and rolling shutter effects, should be considered for future improvements of the model.

6 REFERENCES

[1] M. D. Shuster, S. D. Oh, *Three-Axis Attitude Determination from Vector Observations*, Journal of Guidance and Control, Vol. 4, No. 1, January–February 1981, pp. 70–77.

[2] Wi, J., Baeck, K., and Yoon, H., *Modeling and Filtering Colored Noise of a Star Tracker*, Journal of Astronautical Sciences 70, 8 (2023). https://doi.org/10.1007/s40295-023-00376-w

[3] E. Superfin, D. O'Shaughnessy, D. Mages, M. Jensenius, S. Miller, and M. Pittelkau, *Line of Sight Error Characterization and Mitigations on the DART Mission*, in 2023 AAS Guidance, Navigation, and Control Conference, Breckenridge, CO, February 7, 2023.

[4] Wu, Y.-W., and Li, R., *Star Tracker Error Characteristics and Their Compensation Techniques*, Proceedings of the NASA Goddard Flight Mechanics Symposium, NASA CP-2003-212246, 2003.

[5] Pittelkau, M.E. (2010). Sensors for Attitude Determination. In Encyclopedia of Aerospace Engineering (eds R. Blockley and W. Shyy). https://doi.org/10.1002/9780470686652.eae297

[6] Shi, C.; Zhang, R.; Yu, Y.; Lin, X. *On-Orbit Geometric Distortion Correction on Star Images through 2D Legendre Neural Network*, Remote Sens. 2022, 14, 2814.

[7] Haley DR, *Precision Attitude Estimation with Star Trackers: Experience, Error Models and their Interpretation*, AAS 99-433, in Proc. AAS/AIAA Astrodynamics Specialist Conf., Aug. 1999.

[8] M. Pittelkau, *Distortion and Alignment Calibration of a CCD-Based Fine Sun Sensor*, Flight Mechanics and Estimation Theory Symposium, Goddard Space Flight Center, May 1997, NASA CP3345, pp. 175–187.

[9] Haley DR, and Strikwerda TR, *Experiences in precision attitude determination with the Midcourse Space Experiment (MSX)*, in 1999 Flight Mechanics Symposium Proc., NASA/CP-1999-209235 (20 May 1999).

[10] Markley, F.L., Mortari, D. Quaternion Attitude Estimation Using Vector Observations. J of Astronaut Sci 48, 359–380 (2000). https://doi.org/10.1007/BF03546284

[11] Brown, R.G. and Hwang, P.Y.C. (2012) Introduction to Random Signals and Applied Kalman Filtering with Matlab Exercises. 4th Edition, John Wiley & Sons Inc., Hoboken.

[12] Pittelkau, M. E. *Everything is Relative in Spacecraft System Alignment Calibration*, AIAA Journal of Spacecraft and Rockets, Vol. 39, No. 3, May–June 2002, pp. 460–466.